

## LIST OF FIGURES

1	Jacobian ( $\partial I / \partial P_{\text{LER}}$ ) at Ca K line as a function of pressure for different $\theta_o$ at $R = 65$ and $\theta = 15^\circ$ . . . . .	4
2	Calculated atmospheric (a) and oceanic (b) filling-in at OMI VIS channel spectral resolution, $R = 10\%$ , $\theta_o = 45^\circ$ , nadir-view. . . . .	5
3	Gridded 394.1 nm reflectivity from OMI versus MODIS grid-box mean cloud fraction. The shaded region indicates pixels determined to be partly cloudy (p/c) by both MODIS and OMI (see text for more explanation). . . . .	5
4	Derived corrections ( $K^j(\lambda^i)$ ): Each curve is for a particular scan position. . . . .	7
7	OMI mean grid-box $P_{\text{LER}}$ as a function of the MODIS mean cirrus (high cloud) reflectance. . . . .	8
5	Retrieved gridded cloud parameters from OMI and MODIS on 8 March 2005 . . . . .	9
6	Retrieved gridded cloud parameters from OMI and MODIS on 8 March 2005 . . . . .	10
8	Comparison with MODIS with and without soft calibration. . . . .	11

# First results from the OMI Rotational Raman Scattering Cloud Pressure Algorithm

Joanna Joiner, Alexander Vasilkov

**Abstract**—We have developed an algorithm to retrieve scattering cloud pressures and other cloud properties with the Aura Ozone Monitoring Instrument (OMI). The scattering cloud pressure is retrieved using the effects of rotational Raman scattering (RRS). It is defined as the pressure of a Lambertian surface that would produce the observed amount of RRS consistent with the derived reflectivity of that surface. The independent pixel approximation is used in conjunction with the Lambertian-equivalent reflectivity model to provide an effective radiative cloud fraction and scattering pressure in the presence of broken or thin cloud. The derived cloud pressures will enable accurate retrievals of trace gas mixing ratios, including ozone, in the troposphere within and above clouds. We describe details of the algorithm that will be used for the first release of these products.

We compare our scattering cloud pressures with cloud-top pressures and other cloud properties from the Aqua Moderate-Resolution Imaging Spectroradiometer (MODIS) instrument. OMI and MODIS are part of the so-called A-train satellites flying in formation within 30 minutes of each other. Differences between OMI and MODIS are expected because the MODIS observations in the thermal infrared are more sensitive to the cloud top whereas the backscattered photons in the ultraviolet can penetrate deeper into clouds. Radiative transfer calculations are consistent with the observed differences. The OMI cloud pressures are shown to be correlated with the cirrus reflectance. This relationship indicates that OMI can probe through thin or moderately thick cirrus to lower lying water clouds.

**Index Terms**—cloud, retrieval, Raman, scattering.

## I. INTRODUCTION

PART of the mission of the Ozone Monitoring Instrument (OMI) [1] on NASA's Earth Observing System (EOS) Aura satellite is to continue the 25-year record of high-quality total column ozone retrievals from the Total Ozone Mapping Spectrometer (TOMS). The higher spectral and spatial resolution, coverage, and sampling of OMI, as compared with TOMS will allow for improved ozone retrievals, including estimates of tropospheric ozone as well as retrievals of other trace gases such as SO<sub>2</sub>, NO<sub>2</sub>, BrO, and HCHO [2].

The retrieval of tropospheric ozone has been accomplished with TOMS using cloud-slicing techniques [3], [4]. These methods have been previously implemented using cloud-top pressures derived from thermal infrared (IR) measurements or other assumptions about clouds, *e.g.*, that some highly reflecting clouds either reach close to the tropopause or contain very little tropospheric ozone within and above them. A similar approach [5] has been used with data from the Global Ozone Monitoring Experiment (GOME) [6] aboard the

European Space Agency's (ESA) Second European Remote Sensing Satellite (ERS-2). In that work, cloud pressures were derived simultaneously with GOME using measurements in the oxygen A-band [7], and it was shown that most convective cloud top pressures were between 300 and 500 hPa and do not extend to the tropical tropopause.

Using cloud pressures derived from simultaneous ultraviolet (UV) observations in place of climatological IR cloud-top pressures improves estimates of the above-cloud column ozone [8]. Therefore, it is reasonable to assume that estimates of tropospheric ozone from cloud-slicing will also be improved by using simultaneous measurements in the UV.

Cloud pressures can be retrieved with OMI using either atmospheric rotational Raman scattering (RRS) in the UV [9] or O<sub>2</sub>-O<sub>2</sub> absorption near 477 nm [10]. Both techniques are based on the fact that clouds screen the atmosphere below them from satellite observations. Therefore, clouds reduce the amount of RRS or O<sub>2</sub>-O<sub>2</sub> absorption seen by satellite-borne instruments. Both approaches are being pursued with OMI data. Here, we focus on the RRS retrieval algorithm.

RRS is an inelastic component of molecular scattering in the atmosphere that produces photons that differ in frequency from the incident light. The frequency difference is related to rotational properties of O<sub>2</sub> and N<sub>2</sub> molecules. Approximately 4% of total scattered energy is contained in the RRS lines. The RRS energy is transferred to both longer wavelengths (Stokes lines) and shorter wavelengths (anti-Stokes lines). The RRS wavelength shifts in the UV are of the order of 2 nm.

Rotational Raman scattering (RRS) produces filling-in (depletion) of solar Fraunhofer lines cores (wings). This filling-in, also known as the Ring effect, was first observed in ground-based measurements [11] and later in satellite backscatter observations (*e.g.*, [12]). The Ring effect is present throughout the ultraviolet.

The concept of retrieving cloud pressure using properties of RRS was first demonstrated in [13] using a Lambertian-equivalent reflectivity (LER) cloud model. Later, de Beek *et al.* [14] showed that holding all else constant, the amount of filling-in decreases with increasing cloud optical thickness ( $\tau$ ) for  $\tau < \sim 50$  and saturates for  $\tau > 50$ . The filling-in computed using their Mie scattering radiative transfer model compared well with ground-based measurements and satellite-based observations from GOME.

Joiner *et al.* [9] refined the approach of retrieving a scattering cloud pressure using the LER model with a spectral fitting algorithm and high-spectral resolution GOME measurements. They compared their scattering cloud pressures with coincident measurements from the Along Track Scanning Radiometer-2 (ATSR-2). The differences between the GOME

Manuscript received January 20, 2005; revised November 18, 2005.

J. Joiner is with the National Aeronautics and Space Administration, Goddard Space Flight Center, Greenbelt, MD 20771 USA.

A. P. Vasilkov is with the Science Systems and Applications Inc., Lanham, MD USA.

scattering cloud pressures and the cloud-tops from ATSR-2 were in many cases larger than those simulated by a radiative transfer model with a single cloud deck. A simple model of two cloud decks revealed the potential for significant enhancement of absorption and scattering and provided an explanation for the large GOME-ATSR differences.

The EOS Aura and Aqua are part of the so-called A-train formation of satellites that fly in the same orbit within 30 minutes of each other. The A-train provides an unprecedented opportunity to compare, contrast, understand, and potentially combine information provided by the different sensors. The Aqua Moderate-Resolution Imaging Spectroradiometer (MODIS) provides a wealth of information about cloud properties [15] including the cloud-top pressure, fraction, and phase. Its high spatial resolution enables it to, in some instances, identify multiple cloud decks that may exist within the larger OMI footprint. The Advanced Microwave Scanning Radiometer for the Earth Observing System (AMSR-E), also on Aqua, provides estimates of cloud liquid water [16]. Cloudsat and Calipso are upcoming additions to the formation that will provide more information on cloud vertical profiles.

Here, we review the OMI RRS cloud algorithm and describe post-launch modifications that will be part of the first released version. We begin with brief descriptions of OMI and the EOS Aqua MODIS instruments and data products in section II. The forward radiative transfer model and inverse retrieval algorithm are described in sections III and IV, respectively. We discuss a method to correct for small instrumental anomalies and algorithm effects in section V. Comparisons of OMI scattering cloud pressures with cloud-top pressures from MODIS are shown in section VI. Conclusions and a description of ongoing work are given in section VII.

## II. RELEVANT INSTRUMENT CHARACTERISTICS AND DATA PRODUCTS

### A. OMI

The Ozone Monitoring Instrument (OMI) is a hyperspectral imager with dual grating spectrometers (UV and VIS channels) that employ CCD detectors. The UV channel is further divided into two sub-channels (UV-1 and UV-2). Cloud pressures can be derived with the RRS algorithm using either the UV-2 or VIS channel.

The channels cover 310-365 nm (UV-2) and 365-500 nm (VIS) in the full performance range. In the Global mode that is used for most observations, the swath width is 2600 km with ground pixel sizes of  $13 \times 24$  km at nadir and  $13 \times \sim 128$  km at the largest satellite zenith angle for both the UV-2 and VIS channels. The average nominal spectral resolutions (FWHM) in the Global mode are 0.45 nm (UV-2) and 0.63 nm (VIS), and the average sampling distances are 0.15 nm (UV-2) and 0.23 nm (VIS).

### B. MODIS

MODIS is a 36 channel (band) (0.415-14.235 $\mu$ m) imager that flies on the EOS Terra and Aqua satellites. The spatial resolutions are 250m in 2 bands, 500m in 5 bands, and 1000m in 29 bands. The swath width, 2330 km, is slightly smaller

than OMI's. A detailed description of MODIS is given in [17] that includes the spectral characteristics, pixel size, SNR's, and purpose of each band.

In this paper, we will use several cloud products [18] contained in the level-3 atmosphere product (MOD08) collection 4 [15]. The level-3 data are statistics (*e.g.*, mean, minimum, maximum, standard deviation) that are sorted into  $1^\circ$  latitude  $\times$   $1^\circ$  longitude cells on an equal-angle global grid. For most of the cloud products used here, data are separated into daytime only, nighttime only, or combined day and night. Because OMI only makes scientific measurements in sunlight, we use daytime products from the Aqua MODIS for all comparisons.

The MODIS products shown here include cloud fraction and cloud-top pressure. The cloud fraction is the counts of cloudy and probably cloudy outcomes from the cloud mask algorithm. For the daytime product, this includes information from solar spectral tests as well as a variety of tests performed using infrared channels. The cloud-top pressure is derived with the CO<sub>2</sub> slicing technique that has been detailed in *e.g.*, [19] and [20].

## III. FORWARD MODEL

### A. Lambert-Equivalent Reflectivity (LER) concept

The algorithm utilizes the concept of the Lambert-Equivalent Reflectivity (LER) that is commonly used in trace gas retrieval algorithms. In this approach, a single surface (cloud or ground) is assumed to be opaque and Lambertian with a specified reflectivity. The backscattered radiance,  $I_{TOA}$ , (hereafter assumed to be normalized by the incoming solar irradiance) observed at the top of the atmosphere (TOA) is expressed by

$$I_{TOA} = I_{TOA}(R = 0) + RI_g\gamma/(1 - RS_b), \quad (1)$$

where  $R$  is the surface reflectivity,  $I_g$  is the total radiance reaching the surface,  $\gamma$  is the transmittance of the radiance reflected from the surface, and  $S_b$  is the component of the reflected surface radiance that is scattered by the atmosphere back to the surface. The TOA radiance computed from equation 1 includes only the elastic component.

The Lambert-equivalent reflectivity accounts for the effects of aerosol and cloud scattering and can include light reflection from the ground if the clouds are semi-opaque. The LER concept allows for the treatment of clouds as first suggested in [21]. The LER model treats a cloud as a horizontally homogeneous opaque Lambertian-reflecting surface defined by its reflectivity  $R$  and an effective pressure,  $P_{LER}$ .  $P_{LER}$  is representative of the pressure reached by back-scattered photons averaged over a kernel or weighting function.  $P_{LER}$  is the quantity retrieved with our RRS algorithm using the LER cloud model.

### B. Mixed Lambert-Equivalent Reflectivity (MLER) concept

In the presence of thin or broken cloud, the LER approach can be combined with the independent pixel approximation (IPA). In the IPA, a partly cloudy pixel is assumed to be the sum of clear and cloudy independent sub-pixels weighted according to a cloud fraction  $f$ . This will be referred to as

the Mixed LER (MLER) concept. Following this concept, the observed TOA radiance,  $I_{\text{TOA}}$  can be written in the form:

$$I_{\text{TOA}} = I_{\text{clr}}(1 - f) + I_{\text{cld}}f, \quad (2)$$

where  $I_{\text{clr}}$  and  $I_{\text{cld}}$  are clear and overcast radiances, respectively.  $I_{\text{clr}}$  and  $I_{\text{cld}}$  include both Rayleigh and Raman components that are computed using the assumption of LER surfaces as in (1) with specified ground and cloud reflectivities,  $R_{\text{clr}}$  and  $R_{\text{cld}}$ , respectively, and pressures. The selection of fixed reflectivities for the ground and clouds is somewhat arbitrary. We describe a procedure for selecting  $R_{\text{clr}}$  and  $R_{\text{cld}}$  in section IV-C.

### C. TOMRAD and atmospheric Raman scattering

The forward model used here to compute components of the quantities in (1) at every iteration of scattering is commonly referred to as TOMRAD and is described in more detail in [9]. Briefly, TOMRAD accounts for molecular scattering and specified gaseous absorption using the successive orders of scattering method [22] with corrections for a spherical atmosphere. Raman scattering is computed externally to TOMRAD using the iteration values of the radiance components as in [12], [9]. We have included gaseous absorption in the relatively weak bands of  $\text{O}_2\text{-O}_2$  at 360.4 nm and 380.2 nm using cross-sections from [23].

The filling-in factor is defined as the ratio of the radiance component due to inelastic scattering to that of the elastic scattering. The filling-in is a function of wavelength ( $\lambda$ ), surface pressure ( $P_{\text{LER}}$ ), surface reflectivity ( $R$ ), and satellite viewing geometry that includes the solar zenith angle ( $\theta_o$ ), the viewing or satellite zenith angle ( $\theta$ ), and the relative azimuth angle  $\phi$  (between the solar and satellite viewing angles).

TOMRAD is used to create tables of the iteration values of the radiance components for the relevant wavelengths at 5 LER surface pressures, 10 solar zenith angles, 6 satellite zenith angles, and 7 relative azimuth angles. Using OMI solar spectra measured in the UV-2 and VIS channels, we then create secondary tables that are used to compute the filling in given a value of  $R$ . Separate tables are needed for the UV-2 and VIS channels owing to the different spectral resolutions.

Figure 1 shows the LER pressure Jacobian,  $\partial I(\%)/\partial P_{\text{LER}}(\text{hPa})$ . There is roughly an equal sensitivity of the measurement to  $P_{\text{LER}}$  throughout the troposphere for  $\theta_o \leq 70^\circ$ . For  $\theta_o \leq 45^\circ$  the magnitude of the sensitivity has little dependence on  $\theta_o$ . Sensitivities increase slightly for  $60^\circ \leq \theta_o \leq 77^\circ$ . At higher  $\theta_o$ , sensitivity increases at lower pressures (higher altitudes) while it decreases at higher pressures owing to increasing atmospheric pathlengths.

### D. Ocean Raman scattering

Vibrational Raman scattering by liquid water (ocean Raman scattering) contributes significantly to the filling-in of solar Fraunhofer lines over clear ocean waters for  $\lambda > \sim 350$  nm. The wavelength shifts are much larger than those of atmospheric Raman scattering (mean shift of  $3357 \text{ cm}^{-1}$ ), the band is much wider ( $30\text{-}50 \text{ cm}^{-1}$ ), and the shifts are primarily in the Stokes direction (towards longer wavelengths). A radiative

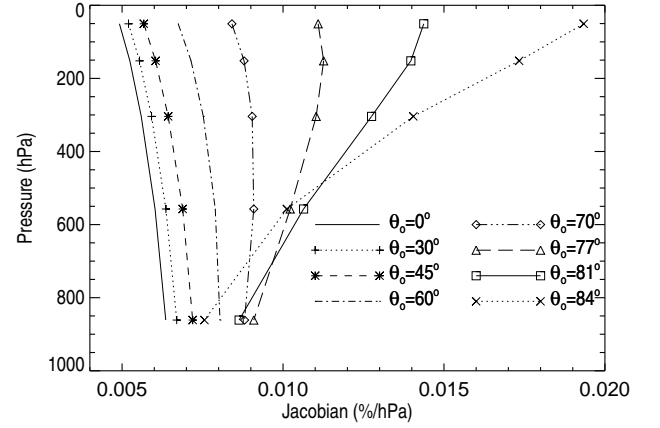


Fig. 1. Jacobian ( $\partial I/\partial P_{\text{LER}}$ ) at Ca K line as a function of pressure for different  $\theta_o$  at  $R = 65$  and  $\theta = 15^\circ$ .

transfer model accounting for this effect has been developed [24] and incorporated into the RRS cloud pressure algorithm. Optical properties of the ocean water are represented through a single input variable: chlorophyll concentration  $C$ . The model was used to generate a lookup table of the oceanic filling-in. The ocean filling-in is a function of  $\theta_o$ ,  $\theta$ , and  $C$ . Since the ocean filling-in is a weak function of the ocean reflectivity, we assume a constant reflectivity of 0.1 in its calculation.

Figure 2 shows the spectral dependence of the fractional filling-in due to both atmospheric and oceanic Raman scattering. The filling-in is calculated using OMI VIS channel solar irradiance data in order to minimize any errors due to uncertainty in the slit function. The spectral signature is similar for the atmospheric and oceanic filling-in. However, the magnitude of the oceanic filling-in is somewhat smaller and decreases with decreasing wavelength owing to reduced amounts of radiance reaching the surface at excitation wavelengths in the ozone Huggins bands. For shorter wavelengths, the ocean filling-in is negative. This represents a net depletion of energy due to the larger energy transfer from those wavelengths to longer wavelengths as compared with the energy gain from shorter wavelengths.

## IV. INVERSION METHOD

### A. Selection of fitting window

We verified that our algorithm performed adequately using both the UV-2 and VIS channels. For the initial release of the RRS cloud products, we have selected a relatively small fitting window in the VIS channel encompassing the Fraunhofer Ca K and H lines (392-398 nm). These very deep lines in the solar spectrum provide a large amount of filling-in and thus the largest signal-to-noise ratio for the RRS cloud pressure algorithm with the fewest wavelengths.

### B. Determination of $R$ and $f$

The Lambert-equivalent reflectivity,  $R$ , is calculated at a single wavelength by direct inversion of (1). For this step, we

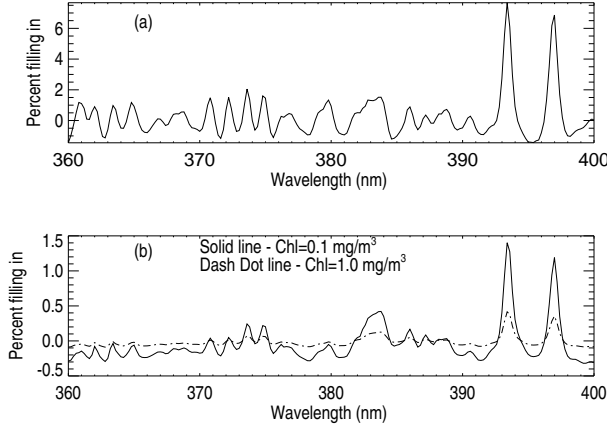


Fig. 2. Calculated atmospheric (a) and oceanic (b) filling-in at OMI VIS channel spectral resolution,  $R = 10\%$ ,  $\theta_o = 45^\circ$ , nadir-view.

use 394.1 nm, a wavelength within our fitting window that is relatively insensitive to RRS.

When  $R_{clr} < R < R_{cld}$ , we invoke MLER and compute a cloud fraction by inverting (2), where  $I_{clr}$  and  $I_{cld}$  are computed using (1) with  $R_{clr}$  and  $R_{cld}$ , respectively. Because we are using fixed values for  $R_{clr}$  and  $R_{cld}$ , we will refer to our retrieved  $f$  as a radiative cloud fraction. In the calculation of  $I_{clr}$ , the LER surface pressure is assumed to be the ground pressure as taken from a climatological terrain database with  $0.5^\circ \times 0.5^\circ$  resolution. For  $I_{cld}$ , we assume  $P_{LER} = 500\text{hPa}$ . The cloud pressure is determined with an iterative algorithm. If the cloud fraction is equal to unity, we recalculate  $R$  at each iteration using the retrieved cloud pressure.

The error in the scattering cloud pressure tends toward infinity as the cloud fraction approaches zero. When the cloud fraction falls below 0.2, we do not attempt to retrieve a cloud pressure with the MLER concept. Instead, for diagnostic purposes, we retrieve a scene pressure using the LER model and flag those pixels accordingly.

### C. Selection of $R_{clr}$ and $R_{cld}$

The choice of the fixed Lambert-equivalent reflectivities for ground (clear-sky)  $R_{clr}$  and cloud  $R_{cld}$  strongly affects the retrieval of the cloud fraction. The OMI total ozone algorithm that is based on the TOMS version 8 (V8) also uses the MLER approach. That algorithm assumes  $R_{clr} = 0.15$  and  $R_{cld} = 0.8$ . The value of  $R_{clr}$  was selected to account for the effects of aerosols [25]. The value of 0.8 for  $R_{cld}$  was chosen to produce the correct amount of Rayleigh scattering [26].

Initially, we planned to use  $R_{cld} = 0.8$  and  $R_{clr} = 0.15$  to be consistent with the TOMS-V8-based OMI total ozone algorithm. However, based on recent discussions with OMI science team members we have adjusted  $R_{cld}$  and  $R_{clr}$ . The new values produce radiative cloud fractions that are closer to geometrical cloud fractions estimated with imagers such as MODIS. This is important for use in retrievals of trace gases, such as  $\text{NO}_2$ , that have a significant component in the lower troposphere. We plan to provide cloud pressures computed with both the new and original values of  $R_{cld}$  and

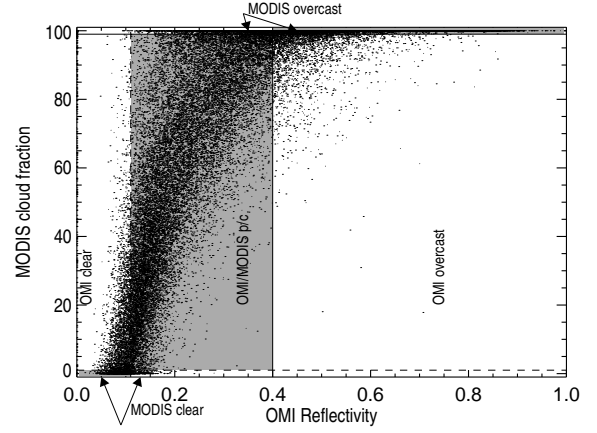


Fig. 3. Gridded 394.1 nm reflectivity from OMI versus MODIS grid-box mean cloud fraction. The shaded region indicates pixels determined to be partly cloudy (p/c) by both MODIS and OMI (see text for more explanation).

$R_{clr}$ . The original values can be used to correct the retrieved total ozone with the TOMS-V8-based OMI algorithm. The cloud fractions and pressures retrieved with the new values would be more appropriate for use with OMI retrievals of tropospheric pollutants such as  $\text{NO}_2$  that have a large boundary layer component.

Figure 3 shows how the 394.1 nm reflectivity compares with the MODIS grid-box mean cloud fraction. In order to derive a value of  $R_{cld}$  consistent with the MODIS cloud fraction, we perform a robustness and power analysis. The solid vertical and horizontal lines in Figure 3 divide it into four quadrants. The solid horizontal line represents the division between MODIS overcast and partly cloudy/clear pixels (drawn just below 100% for clarity). The vertical line, shown at a value of  $R = 0.4$ , represents the division between OMI overcast and partly cloudy/clear derived using that value of  $R_{cld}$ . The robustness refers to the ability to correctly identify a pixel as either overcast or partly cloudy (e.g., points in the upper right or lower left quadrants) for a given value of  $R_{cld}$ . The power refers to the ability not to err by identifying an overcast pixel as partly cloudy or vice-versa.

In table I, we compute the percentages of pixels that fall into the four quadrants for a range of  $R_{cld}$ . The average error (average of columns 3 and 5) has minimum at  $R_{cld} = 0.4$ . We select 0.4 for  $R_{cld}$  based on this criteria. We perform a similar analysis for  $R_{clr}$  yielding a value of 0.11. An example of the four quadrants used to derive  $R_{clr}$  are indicated in Figure 3 by the dashed lines. The selected values of  $R_{cld}$  and  $R_{clr}$  produce a bias (standard deviation) in the radiative cloud fraction, with respect to MODIS, of -0.216 (0.221) and a correlation coefficient of 0.82.

### D. Determination of scattering cloud pressure ( $P_{LER}$ )

The algorithm retrieves  $P_{LER}$  by spectrally fitting the observed high-frequency structure of  $I_{TOA}$  using the radiative transfer model described above. The TOA radiance is assumed to take the general form:

$$I_{TOA} = A_0 + A_1\lambda + r(\lambda, R, P_{LER}, \theta_0, \theta, \phi, C). \quad (3)$$

TABLE I

POWER AND ROBUSTNESS ANALYSIS OF OMI OVERCAST (OVC) AND PARTLY CLOUDY/CLEAR (P/C) DETECTION USING MODIS (MOD) AS THE REFERENCE (SEE TEXT FOR MORE EXPLANATION).

$R_{\text{cld}}$	OMI ovc MOD ovc	OMI p/c MOD ovc	OMI p/c MOD p/c	OMI ovc MOD p/c	Avg error
0.20	97.8	2.2	48.3	51.7	27.0
0.25	95.9	4.1	60.0	40.0	22.0
0.30	93.1	6.9	69.6	30.4	18.6
0.35	89.3	10.7	77.9	22.1	16.4
0.40	84.4	15.6	84.8	15.2	15.4
0.45	77.6	22.4	90.0	10.0	16.2
0.50	68.5	31.5	93.9	6.1	18.8
0.55	57.9	42.1	96.4	3.6	22.9
0.60	46.0	54.0	98.1	1.9	28.0
0.65	34.0	66.0	99.0	1.0	33.5
0.70	23.1	76.9	99.5	0.5	38.7
0.75	14.9	85.1	99.8	0.2	42.7
0.80	8.3	91.7	99.9	0.1	45.9

where  $A_0$  and  $A_1$  are coefficients that define the low frequency component of the observed radiance and  $r$  represents the high-frequency component that includes atmospheric and oceanic Raman scattering as well as gaseous absorption. In general,  $r$  depends on the LER parameters  $R$  and  $P_{\text{LER}}$  as well as on the satellite viewing geometry as described above and optionally the chlorophyll concentration,  $C$ . In accordance with MLER, we compute  $r$  at a given wavelength and satellite geometry as the sum of clear and cloudy components,  $r_{\text{clr}}$  and  $r_{\text{cld}}$ , respectively, weighted appropriately using  $f$ , *i.e.*,

$$r = r_{\text{clr}}(R_{\text{clr}}, P_s)(1 - f) + r_{\text{cld}}(R_{\text{cld}}, P_{\text{cld}})f, \quad (4)$$

where  $P_s$  and  $P_{\text{cld}}$  are the surface and cloud LER pressures, respectively.

We use two coefficients ( $A_0$  and  $A_1$ ) to form a linear fit of the low-frequency component of radiance that accounts for Rayleigh and aerosol scattering. This is sufficient for our relatively narrow spectral fitting window. For a larger wavelength range such as used in [9], a quadratic term may be required.

The cloud pressure is retrieved by an iterative minimum-variance (least-squares) procedure using

$$x_{n+1} = x_n + (H_n^T O^{-1} H_n + B^{-1})^{-1} (H_n^T O^{-1} [y^{\text{obs}} - y_n^{\text{calc}}] + B^{-1} [x_n - x_0]), \quad (5)$$

where  $x_n$  is state vector estimate at iteration  $n$ ,  $H$  is the Jacobian matrix (partial derivatives of the observable with respect to the state vector),  $O$  is the observation error covariance that includes measurement and forward model error,  $y^{\text{obs}}$  and  $y^{\text{calc}}$  are vectors of observed and calculated radiances, respectively,  $B$  is the background (first guess) error covariance, and  $T$  denotes transpose.

Components of the state vector  $x$  include  $A_0$ ,  $A_1$ ,  $P_{\text{LER}}$ , and a wavelength shift term that accounts for small differences in wavelength between the solar and Earth-view spectra. Joiner *et al.* [9] found that a spectral squeeze term was needed for fitting GOME data with a wider fitting window. We have found that this is not necessary for OMI using the relatively narrow window.

Chlorophyll concentration,  $C$ , can optionally be added to the state vector over oceans, but is currently not included. Instead, for clear and partially cloudy pixels, ocean Raman scattering is computed using an annual mean climatology from the Sea-viewing Wide Field-of-view Sensor (SeaWiFS) [27]. Note that when the cloud fraction is small, the climatology overestimates  $C$ , and  $C$  is small ( $< \sim 0.2 \text{ mg/m}^3$ ), the retrieved cloud pressure can be too high and may be greater than the surface pressure.

The background error covariance,  $B$ , is nominally a diagonal matrix with large values on the diagonal for all parameters retrieved here. It has been included for the general case where chlorophyll is included. The background constraint is necessary when chlorophyll is included, because the sensitivity to chlorophyll is relatively low for high chlorophyll amounts.

The observation vector,  $y^{\text{obs}}$  includes normalized radiances interpolated to the table wavelengths that have a 0.2 nm spacing. The observation error covariance,  $O$ , matrix is a diagonal matrix with the square root diagonal set to 0.5% of the observed value. This value of 0.5% includes both radiometric noise and forward modeling errors. Because the same value is used for all wavelengths and the background errors are set to large values, the chosen value of 0.5% does not affect the retrievals.

Occasionally, a transient event can occur in an isolated pixel, *e.g.*, from a radiation hit, causing a spike in the observation. If not accounted for, this results in an intermittent stripe in a retrieved product. After the initial fit in the first iteration, we eliminate every member of the observation vector with an absolute difference of more than 6% from the calculated value.

After a number of hits, a pixel may become permanently hot or may remain hot for a long period with elevated dark currents. The effects of hot pixels are mitigated by periodically updating dark current maps. Transients and hot pixels affect measured solar irradiances much more than the Earth radiance because solar signal levels are approximately 2 orders of magnitude less. In order to minimize the effects of transients and permanently hot pixels, we have chosen to use a single OMI solar irradiance file to compute all normalized radiances. We selected the solar spectrum of orbit 2327 on 22 December 2004. Dark current maps are presently updated for calibration approximately once per month. We selected this solar spectrum because it was taken just after a dark current update. In addition, it was taken on a date that minimizes goniometry errors. We then account for changes in the Earth-Sun distance relative to this date in our processing.

## V. SOFT CALIBRATION

For accurate cloud pressures, we found it necessary to apply small calibration adjustments (typically less than 1%) to each detector element, *i.e.*, each wavelength  $i$  and scan position  $j$ . This procedure reduces systematic cross-track errors that may appear as “striping” across the satellite swath as will be shown in section VI. The general approach is to use our radiative transfer model to compute radiances for scenes where we assume that all parameters are known, *e.g.*, cloud-free pixels ( $P = P_s$ ) where  $R_{\text{clr}}$  is specified.

Here, we assume that the corrections take the form of a multiplicative error, *i.e.*,

$$I_{\text{calc}}^{i,j} = K^{i,j} I_{\text{obs}}^{i,j}, \quad (6)$$

where  $I_{\text{obs}}^{i,j}$  and  $I_{\text{calc}}^{i,j}$  are observed and calculated radiances, respectively, and  $K^{i,j}$  are the correction factors. In this work,  $I_{\text{obs}}^{i,j}$  and  $I_{\text{calc}}^{i,j}$  include only the high-frequency component of the radiance. In general, they could also be applied to the total radiance. It should be noted that a multiplicative constant can account for additive errors in the solar spectrum used to compute normalized radiances. Since we use a constant solar spectrum, when we take the radiance to irradiance ratio, an additive error,  $\epsilon$ , in the solar irradiance will produce a denominator of the form  $F + \epsilon$ , where  $F$  is the true solar flux. The denominator can also be written in the form  $F(1 + \delta)$ , where the error is now represented as a multiplicative constant  $(1 + \delta)$ . This error may now be accounted by deriving corrections of the form given in equation 6.

To determine  $K^{i,j}$ , we have selected pixels over highly reflecting ice-covered land whose reflectivities are relatively constant and Lambertian [28]. In particular, the Antarctic plateau region has the highest surface reflectivity, low aerosol loading during quiescent periods, and the least amount of cloud cover [28]. One disadvantage of using Antarctic data for soft calibration is that due to the inclination of the Aura satellite, there is limited data for some scans positions at certain times of the year.

This work uses the latest version of OMI level 1b (L1b) processing as of September 2005 (referred to as GDPS0.9.13). Here, we use 2 days of reprocessed data near solstice in December of 2004 to compute the corrections. In this work, we use pixels with  $\theta_o$  up to  $84^\circ$ . These data are not recommended for soft-calibration of total normalized radiance [S. Taylor, *priv. comm.*]. However, they appear to be adequate for soft-calibration of the high-frequency component of the radiance as will be shown in section VI.

Figure 4 shows the spectral corrections for different scan positions. An overall envelope is apparent with a few scan positions having larger adjustment factors at a few wavelengths. Corrections in the envelope are due primarily to errors caused by linearly interpolating the OMI normalized radiances to the predefined table wavelengths. Note that the OMI wavelengths vary as a function of scan position.

In our algorithm, we have chosen to interpolate the observations at all scan positions to a consistent wavelength grid for fitting. We simulated the interpolation error by convolving a high spectral resolution solar spectrum with a simulated OMI slit function. We found that the general characteristics of the simulated errors (shape and magnitude) were similar to the corrections shown in figure 4. Although it is possible to model these errors [29], the soft-calibration approach appears to adequately correct them. Using a spline interpolation reduces the errors, but causes more data to be lost from the fit when there are missing or bad pixels.

## VI. RESULTS AND COMPARISON WITH MODIS

The high spatial resolution of both OMI and MODIS and their close collocation in time (due to formation flying) allows

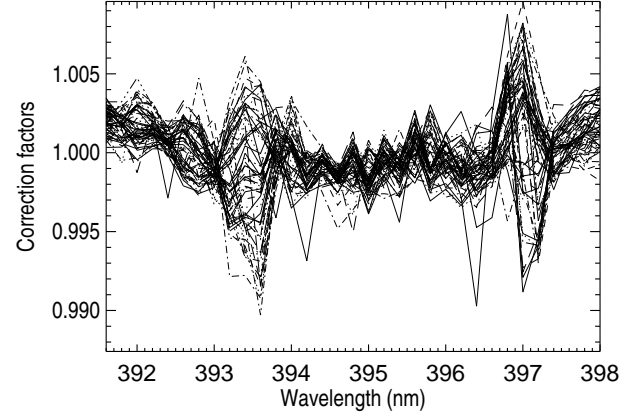


Fig. 4. Derived corrections ( $K^j(\lambda^i)$ ): Each curve is for a particular scan position.

TABLE II

STATISTICS FOR DIFFERENT OMI  $P_{\text{LER}}$  AND MODIS  $P_{\text{top}}$  GRID-BOX AVERAGES (ALL PRESSURES ARE IN hPa) FOR ALL ORBITS OF 08 MARCH 2005 (SEE TEXT FOR MORE EXPLANATION).

OMI box	MODIS box	Case*	No. of sampl.	OMI $P_{\text{LER}}$	MODIS $P_{\text{top}}$	$\Delta P$ mean
Mean	Mean	1	6995	721	522	199
Mean	Mean	2	2187	722	518	204
Mean	Mean	3	2006	717	530	187
Mean	Mean	4	1215	803	626	176
Mean	Mean	5	369	614	324	290
Max	Max	1	6995	816	693	124
Max	Max	2	2187	855	772	83
Max	Max	3	2006	777	618	159
Max	Max	4	1215	882	891	-9
Max	Max	5	369	803	442	360
Min	Min	1	6995	631	390	241
Min	Min	2	2187	593	338	255
Min	Min	3	2006	662	463	199
Min	Min	4	1215	720	368	353
Min	Min	5	369	449	257	192

\*Case 1: All good matchups; Case 2:  $\sigma_{\text{OMI}} > 50$ ,  $\sigma_{\text{MODIS}} > 50$ ; Case 3:  $\sigma_{\text{OMI}} < 50$ ,  $\sigma_{\text{MODIS}} < 50$ ; Case 4:  $\sigma_{\text{OMI}} - \sigma_{\text{MODIS}} < -50$ ; Case 5:  $\sigma_{\text{OMI}} - \sigma_{\text{MODIS}} > 50$ ; where  $\sigma$  denotes grid-box standard deviation.

for the most detailed comparison between the two types of cloud pressure retrievals to date. In this section, we have averaged cloud pressures ( $P_{\text{LER}}$ ) from OMI in the same  $1^\circ \times 1^\circ$  grid-boxes as the MODIS level 3 products for all daytime orbits of March 8, 2005. We use only grid-boxes where OMI reports a cloud fraction of unity and MODIS reports a cloud fraction of at least 0.97. This avoids confusion due to the cloud fraction effect described in section IV-C. Statistics are computed using data between latitudes of  $70^\circ$  S and  $70^\circ$  N.

Table II lists averages of the grid-box means, maxima (max), and minima (min) for the OMI  $P_{\text{LER}}$ , the MODIS  $P_{\text{top}}$ , and the difference between the two referred to as  $\Delta P$ , for a variety of different samples. In order to provide further insight into the differences between OMI and MODIS, the statistics are broken down into five subsets that are based on the amount of grid-box variability observed with both instruments. High variability from one or both instruments indicates the presence of multiple or hidden cloud decks within a grid-box.

The first subset includes all good collocations. The second (third) subset includes only those grid-boxes where both OMI and MODIS see high (low) grid-box variability as indicated by a grid-box standard deviation,  $\sigma$ , greater (less) than 50 hPa. The fourth (fifth) subset includes only data where MODIS (OMI) grid-box variability is significantly greater ( $> 50$  hPa) than that of OMI (MODIS). The number of samples meeting the criteria for each case is also given. Standard deviations of the differences for all cases were relatively similar and in the range of 100-150 hPa.

The geographic distributions of OMI and MODIS grid-box cloud pressure standard deviations are shown in figure 5(e)-(f), respectively. The differences between the OMI and MODIS grid-box standard deviations are highlighted in figure 6(d). MODIS occasionally observes higher variability (case 4, blue pixels in figure 6(d)) especially at the edges of frontal systems. Less frequently, OMI has higher variability (case 5, red pixels in figure 6(d)). Case 5 occurs almost exclusively in tropical convective areas.

In general, the mean of  $\Delta P$  is positive, *i.e.*, OMI  $P_{LER}$  is on average greater than the MODIS  $P_{top}$ . Similar results have been previously reported with different sets of UV and IR instruments [13], [9]. The large mean value of  $\Delta P$  has been explained by radiative transfer modeling that shows significant light penetration into clouds that varies with cloud optical and geometrical thickness [14], [9], [26]. Scattering and absorption approaches to retrieve  $P_{LER}$  will therefore report higher pressures (lower altitudes) than the physical cloud top. A second explanation for the relatively large differences is the existence of multiple cloud decks. It has been shown that the effect of a second optically thick cloud deck can be significant for an upper deck with cloud optical thickness  $\tau < \sim 25$  [9].

While the average difference in the grid-box means is relatively large ( $\sim 200$  hPa for cases 1-4), average differences between the grid-box maxima are smaller for cases 1-4. When multiple cloud decks are inferred by both instruments as indicated by high grid-box variability ( $\sigma > 50$  hPa, case 2), the average difference between the OMI and MODIS grid-box maxima is about half that when grid-box variability is small (case 3). The better agreement for case 2, where the presence of multiple cloud decks is indicated by both instruments, suggests that MODIS may be seeing through holes in or around edges of cirrus clouds that OMI has little sensitivity to. In these cases, MODIS reports grid-box maxima more representative of lower level water clouds that OMI is more sensitive to. Conversely, when there is little variability observed by both MODIS and OMI, MODIS may not be seeing through high layers of cirrus.

Figure 5(a)-(b) maps the OMI grid-box maximum  $P_{LER}$  and the MODIS grid-box maximum  $P_{top}$ , respectively. Similarly, figure 5(c)-(d) shows the grid-box minima. The OMI-MODIS differences in the grid-box maxima, minima, and means are shown in figure 6(a)-(c).

These figures show clearly that MODIS often sees higher altitude clouds in the mid-latitude storm tracks. Retrievals of cloud liquid water from AMSR-E, not shown here, reveal that frontal systems where MODIS reports high-altitude cirrus also have clouds with large amounts of liquid water. The

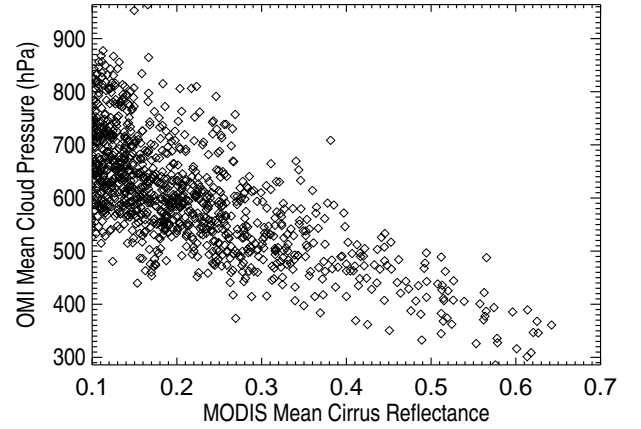


Fig. 7. OMI mean grid-box  $P_{LER}$  as a function of the MODIS mean cirrus (high cloud) reflectance.

OMI reflectivities, shown in 6(e), can be quite high for these systems, further indicating clouds with a substantial amount of liquid water. Because the MODIS cirrus reflectances, shown in 6(f), are in the low to middle range ( $< \sim 0.45$ ) for these clouds, OMI partially sees through the cirrus and reports a pressure more representative of that of water clouds. Examination of the MODIS grid-box standard deviations in figure 5(f) shows that it is not uncommon for MODIS to see only high clouds (*i.e.*, low grid-box variability and low grid-box maximum pressure) in the frontal regions.

For cases 1-4, the OMI minimum  $P_{LER}$  is significantly higher than the MODIS minimum  $P_{top}$ . This again suggests that OMI is less sensitive than MODIS to optically thin cirrus.

When MODIS has higher grid-box variability than OMI (case 4), the average OMI-MODIS difference in the grid-box maximum cloud pressure is practically negligible. In this case, it is likely that both OMI and MODIS are sensing the same relatively uniform lower cloud deck. These situations occur primarily at middle and high latitudes.

When OMI has higher variability than MODIS (case 5), which primarily occurs in convective regions, there is a large average difference between the OMI and MODIS grid-box maximum cloud pressure and a smaller bias between grid-box minimum. These grid-boxes may have clouds with variable geometrical thicknesses or variable lower layers underneath a more uniform upper cloud deck.

OMI retrieves high clouds infrequently (about 1% of the grid-boxes shown here) and these occur almost exclusively in the tropics as indicated by the distribution of grid-box cloud pressure minima in figure 5(c). There is a strong correlation between pressures of the higher convective clouds and the MODIS cirrus reflectance product retrieved with visible and near-IR water vapor absorbing channels [30] shown in 6(f). Although the product is named cirrus reflectance, it is more indicative of generic high cloud reflectance where the cloud may also be composed of liquid water. The correlation between the OMI  $P_{LER}$  and cirrus reflectance is shown more clearly in Figure 7. OMI primarily retrieves high clouds only when



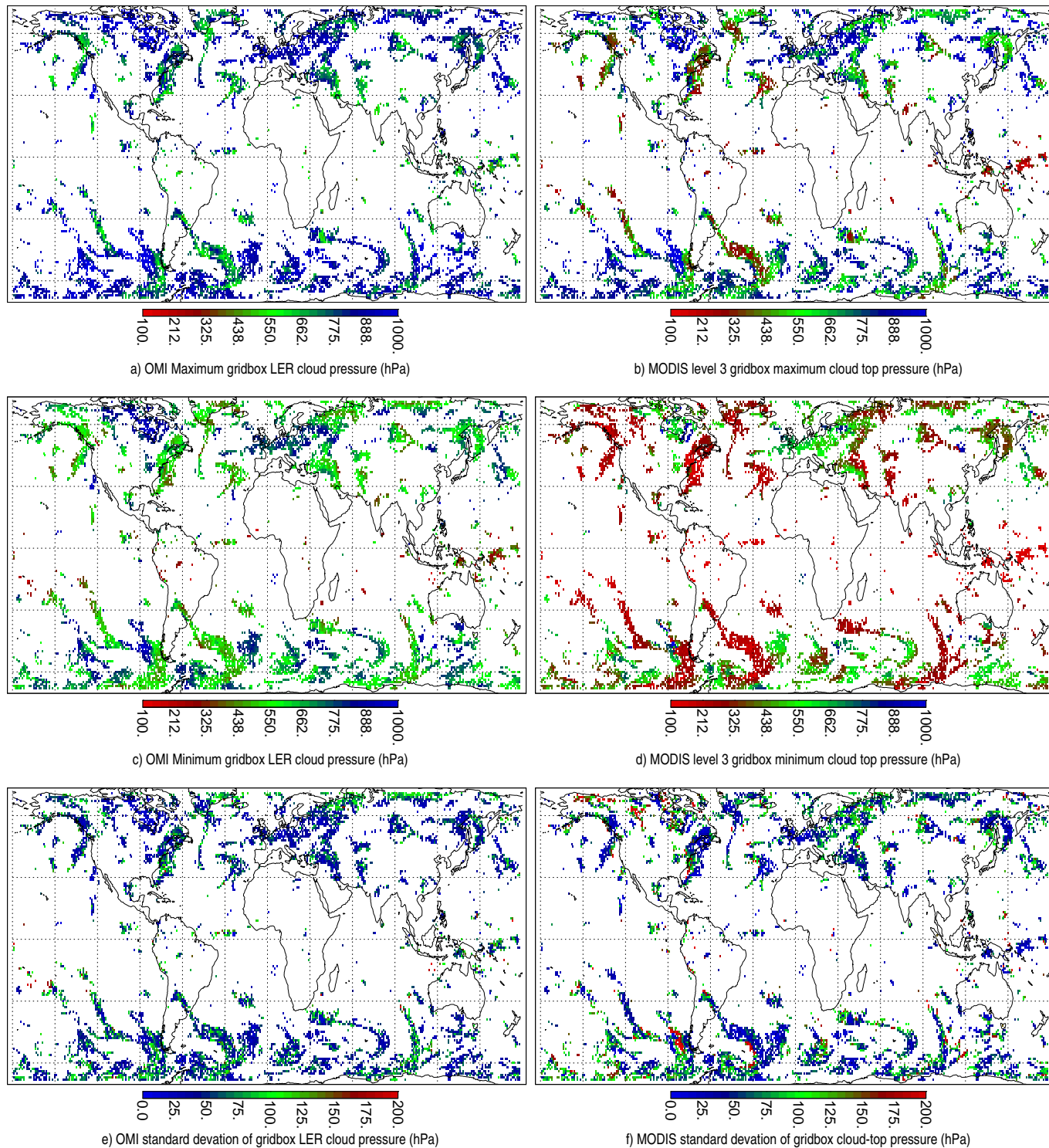


Fig. 5. Retrieved gridded cloud parameters from OMI and MODIS on 8 March 2005

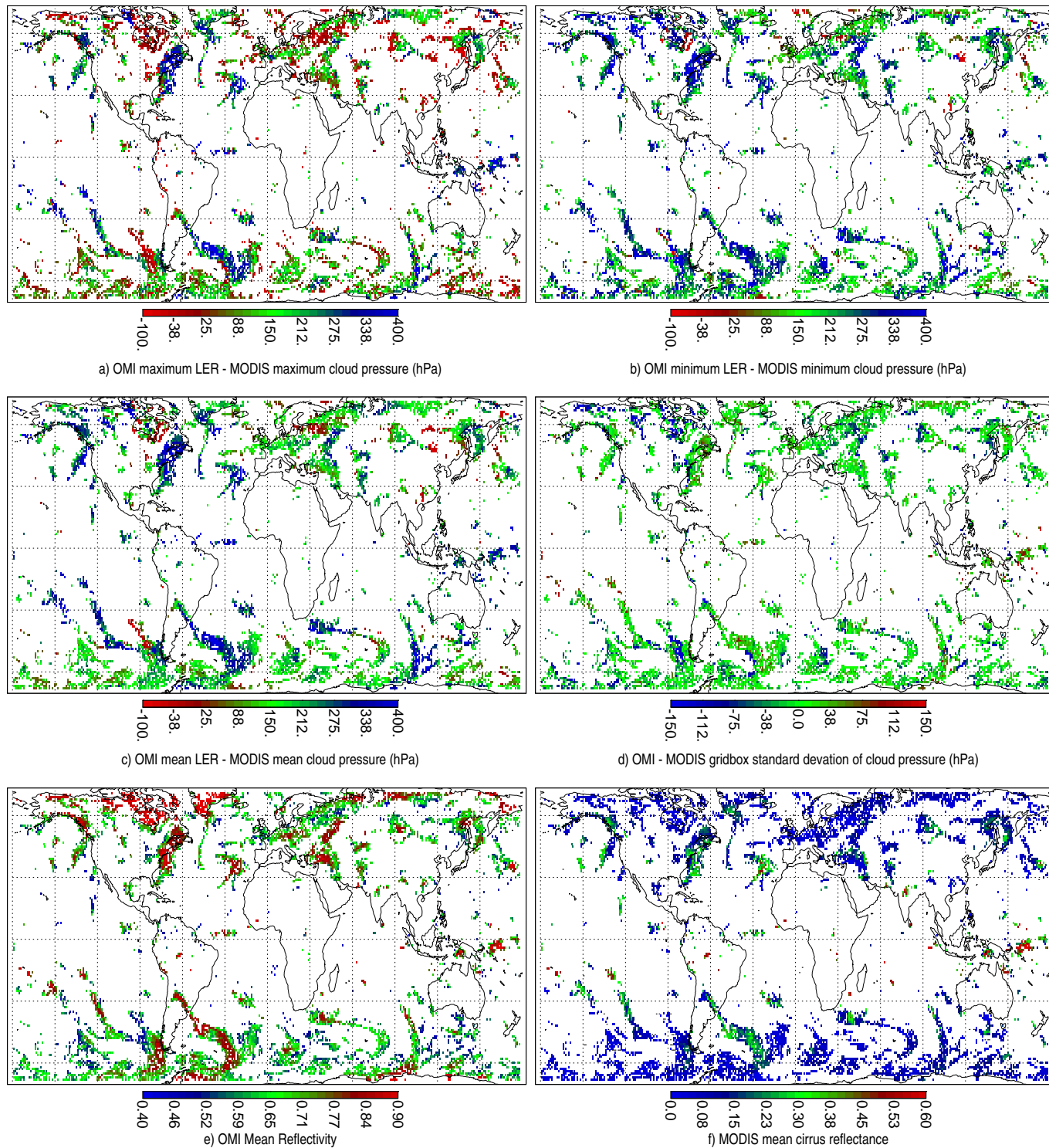


Fig. 6. Retrieved gridded cloud parameters from OMI and MODIS on 8 March 2005

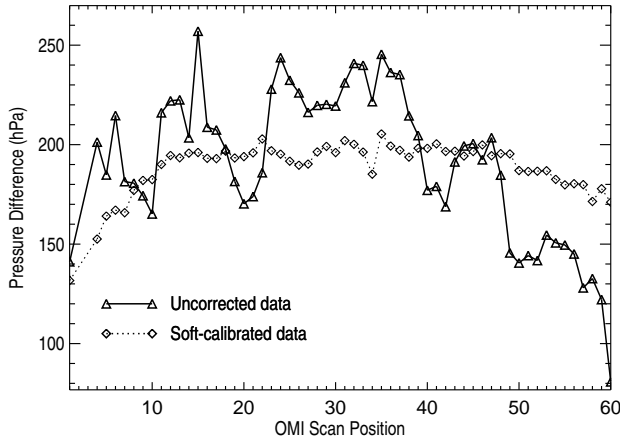


Fig. 8. Comparison with MODIS with and without soft calibration.

the cirrus reflectivity is in the high range ( $> \sim 0.45$ ).

Ahmad *et al.* [26] have suggested that UV light may penetrate substantially into deep convective clouds. For convective clouds, we found a mean difference between the minimum grid-box  $P_{\text{LER}}$  and  $P_{\text{top}}$  of 137 hPa with a standard deviation of 49 hPa. This suggests that light penetration into deep convective clouds is significant. This comparison was based on 34 low latitude samples where both the OMI and MODIS minimum grid-box cloud pressures were less than 300 hPa and the maximum OMI grid-box reflectivity was greater than 0.7.

Finally, we evaluate the soft-calibration by comparing our retrieved cloud pressures with MODIS as a function of scan position in Figure 8. Here, we plot the mean of the difference between single OMI pixel  $P_{\text{LER}}$  and the closest MODIS grid-box mean  $P_{\text{top}}$  for each scan position. The bumps in the uncorrected data (*i.e.*, striping) are largely removed by the soft calibration. The trailing off of the differences at the left swath edge is primarily due to the collocation criteria matching OMI pixels to MODIS grid-boxes that contain data from different orbits. This occurs at higher latitudes owing to the fact that the OMI swath is larger than that of MODIS and asymmetric with respect to the spacecraft nadir due to small asymmetry of the instrument optical axis.

## VII. CONCLUSIONS AND ONGOING WORK

This work documents elements of the first version of the OMI cloud products derived from rotational Raman scattering. The original (prelaunch) estimates of the accuracy and precision of the effective cloud pressure retrieval were 100 and 30 hPa, respectively. Traditional validation of the retrieved scattering cloud pressures and radiative cloud fractions is difficult owing to the fact that these are different from the true cloud top and geometrical cloud fraction. Our preliminary comparisons with MODIS are consistent with radiative transfer calculations that show a large enhancement in scattering from multiple cloud decks and significant light penetration into deep convective clouds. We can estimate the precision of the cloud pressure retrieval with a linear error analysis as in [9]. Using a conservative estimate of 0.5% for the normalized

radiance precision, we find that a cloud pressure precision of better than 30 hPa is obtained at all solar zenith angles when the cloud fraction is 100%. Based on these comparisons and considerations, we believe that our original error estimates are reasonable.

We have chosen a Lambertian-equivalent reflecting model to represent an effective cloud pressure that approximates an average pressure reached by backscattered solar photons. A more realistic treatment of clouds using full Mie scattering radiative transfer will be considered in the future. We plan to evaluate whether this will significantly improve trace-gas retrievals. Note that a change to this type of cloud treatment will have to be done in coordination with the other trace-gas retrieval algorithms.

We are currently examining our OMI cloud pressure retrievals and those of MODIS where we have collocations with the Cloud Physics Lidar (CPL) that flew on the WB-57 aircraft as part of the Aura Validation Experiment (AVE) in fall of 2004. It is hoped that this type of comparison will enable a better understanding of the differences between  $P_{\text{top}}$  from IR measurements and  $P_{\text{LER}}$  from scattering and absorption approaches in the presence of single and multiple cloud decks. Observations from Cloudsat and Calipso, to be launched in late 2005 or early 2006, will provide further insight. The ultimate goal is to combine measurements from passive sensors in the microwave, IR, VIS, and UV to produce information on cloud vertical extent and the existence and pressures of multiple cloud decks.

## ACKNOWLEDGMENT

The authors thank members of the OMI science and processing team including P.K. Bhartia, P. Levelt, E. Hilsenrath, S. Chandra, J. Ziemke, E. Bucsela, D. Flittner, R. McPeters, P. Veefkind, P. Stammes, J. de Haan, G. Jaross, T. Kelly, R. Cebula, S. Taylor, and M. Hopkins for helpful discussions and assistance with OMI data. This work was supported by NASA through funding for the EOS Aura OMI science team.

## REFERENCES

- [1] Levelt, P., G.H.J. van den Oord, M.R. Dobber, A. Malkki, H. Visser, J. de Vries, P. Stammes, J. Lundell, and H. Saari, "The Ozone Monitoring Instrument," *IEEE Trans. Geosci. Rem. Sens.*, this issue, 2006.
- [2] Levelt, E. Hilsenrath, G.W. Leppelmeier, G.H.J. van den Oord, P.K. Bhartia, J. Tamminen, J.F. de Haan, and J.P. Veefkind, "Science Objectives of the Ozone Monitoring Instrument," *IEEE Trans. Geosci. Rem. Sens.*, this issue, 2006.
- [3] J. R. Ziemke, S. Chandra, and P. K. Bhartia, "Cloud slicing: A new technique to derive upper tropospheric ozone from satellite measurements," *J. Geophys. Res.*, vol. 106, pp. 9853–9867, 2001.
- [4] J. R. Ziemke, S. Chandra, and P. K. Bhartia, "Two new methods for deriving tropospheric column ozone from TOMS measurements: Assimilated UARS MLS/HALOE and convective-cloud differential techniques," *J. Geophys. Res.*, vol. 103, pp. 22115–22127, 1998.
- [5] P.J.M. Valks, R.B.A. Koelemeijer, M. van Weele, P. van Velthoven, J.P.F. Fortuin, and H. Kelder, "Variability in tropical tropospheric ozone: Analysis with Global Ozone Monitoring Experiment observations and a global model," *J. Geophys. Res.*, vol. 108, doi: 10.1029/2002JD002894, 2003.
- [6] Burrows, J. P. *et al.*, "The Global Ozone Monitoring Experiment (GOME): Mission concept and first scientific results," *J. Atmos. Sci.*, vol. 56, pp. 151–171, 1999.

- [7] R. B. A. Koelemeijer, P. Stammes, J. W. Hovenier, and J. F. de Haan, "A fast method for retrieval of cloud parameters using oxygen A band measurements from the GOME," *J. Geophys. Res.*, vol. 106, pp. 3475–3490, 2001.
- [8] A. P. Vasilkov, J. Joiner, K. Yang, and P. K. Bhartia, "Improving total column ozone retrievals by using cloud pressures derived from Raman scattering in the UV," *Geophys. Res. Letters*, vol. 31, L20109, doi:10.1029/2004GL020603, 2004.
- [9] J. Joiner, A.P. Vasilkov, D.E. Flittner, J.F. Gleason, and P.K. Bhartia, "Retrieval of cloud pressure and oceanic chlorophyll content using Raman scattering in GOME ultraviolet spectra," *J. Geophys. Res.*, vol. 109, D01109, doi:10.1029/2003JD003698, 2004.
- [10] J.R. Acarreta, J.F. de Haan, and P. Stammes, "Cloud pressure retrieval using the O<sub>2</sub>-O<sub>2</sub> absorption band at 477 nm," *J. Geophys. Res.* vol. 109, D05204, doi: 10.1029/2003JD003915, 2004.
- [11] J.F. Grainger and J. Ring, "Anomalous Fraunhofer line profiles," *Nature*, vol. 193, p. 762, 1962.
- [12] J. Joiner, P.K. Bhartia, R.P. Cebula, E. Hilsenrath, R.D. McPeters, and H. Park, "Rotational Raman scattering (Ring effect) in satellite backscatter ultraviolet measurements," *Appl. Opt.*, vol. 34, pp. 4513–4525, 1995.
- [13] J. Joiner and P.K. Bhartia, "The determination of cloud pressure from rotational Raman scattering in satellite backscatter ultraviolet measurements," *J. Geophys. Res.*, vol. 100, pp. 23019–23026, 1995.
- [14] de Beek R., Vountas, M., Rozanov, V. V., Richter, A., and J. P. Burrows, "The ring effect in the cloudy atmosphere," *Geophys. Res. Lett.*, vol. 28, pp. 721–724, 2001.
- [15] M. D. King, W. P. Menzel, Y. J. Kaufman, D. Tanré, B.-C. Gao, S. Platnick, S. A. Ackerman, L. A. Remer, R. Pincus, and P. A. Hubanks, "Cloud and aerosol properties, precipitable water, and profiles of temperature and water vapor from MODIS," *IEEE Trans. Geosci. Rem. Sens.*, vol. 41, pp. 442–458, 2003.
- [16] T. Kawanishi *et al.*, "The Advanced Microwave Scanning Radiometer for the Earth Observing System (AMSR-E), NASA's contribution to the EOS for global energy and water cycle studies," *IEEE Trans. Geosci. Rem. Sens.*, vol. 41, pp. 184–194, 2003.
- [17] W. L. Barnes, T. S. Pagano, and V. V. Salomonson, "Prelaunch characteristics of the MODerate Resolution Imaging Spectroradiometer (MODIS) on EOS-AM1," *IEEE Trans. Geosci. Rem. Sens.*, vol. 36, pp. 1088–1100, 1998.
- [18] S. Platnick, M. D. King, S. A. Ackerman, W. P. Menzel, B. A. Baum, J. C. Riédi, and R. A. Frey, "The MODIS cloud products: algorithms and examples from Terra," *IEEE Trans. Geosci. Rem. Sens.*, vol. 41, pp. 459–473, 2003.
- [19] W. P. Menzel, D. P. Wylie, and K. I. Strabala, "Seasonal and diurnal changes in cirrus clouds as seen in four years of observations with the VAS," *J. Appl. Meteorol.*, vol. 31, pp. 370–385, 1992.
- [20] D. P. Wylie, W. P. Menzel, H. M. Woolf, and K. I. Strabala, "Four years of global cirrus cloud statistics using HIRS," *J. Clim.*, vol. 7, pp. 1972–1986, 1994.
- [21] C. Mateer, D. F. Heath, and A. J. Kruger, "Estimation of total ozone, from satellite measurements of backscattered ultraviolet Earth radiance," *J. Atmos. Sci.*, vol. 28, pp. 1307–1311, 1971.
- [22] J. V. Dave, "Meaning of successive iteration of the auxiliary equation in the theory of radiative transfer," *Astrophys. J.*, vol. 140, pp. 1292–1303, 1964.
- [23] Greenblatt, G. D., Orlando, J. J., Burkholder, J. B., and A. R. Ravishankara, "Absorption measurements of oxygen between 330 and 1140 nm," *J. Geophys. Res.*, vol. 95, pp. 18577–18582, 1990.
- [24] A. P. Vasilkov, J. Joiner, J. Gleason, and P. K. Bhartia, "Ocean Raman scattering in satellite backscatter UV measurements," *Geophys. Res. Letters*, vol. 29, 1837, doi:10.1029/2001GL014933, 2002.
- [25] P. K. Bhartia and C. W. Wellemeyer, "TOMS-V8 Total O<sub>3</sub> Algorithm, OMI Algorithm Theoretical Basis Document," vol. 2, ed. by P.K Bhartia, [http://toms.gsfc.nasa.gov/version8/v8toms\\_atbd.pdf](http://toms.gsfc.nasa.gov/version8/v8toms_atbd.pdf) Greenbelt, Md, 2002.
- [26] Z. Ahmad, P. K. Bhartia, and N. Krotkov, "Spectral properties of backscattered UV radiation in cloudy atmospheres," *J. Geophys. Res.*, vol. 109, D01201, doi:10.1029/2003JD003395, 2004.
- [27] S. B. Hooker, W. E. Esais, G. C. Feldman, W. W. Gregg, and C. R. McClain, "An overview of SeaWiFS and ocean color", SeaWiFS Technical Report Series, Vol. 1, NASA Goddard Space Flight Center, Greenbelt, MD, USA, 1992.
- [28] G. Jaross, A. J. Krueger, and D. Flittner, "Multispectral calibration of remote-sensing instruments over Antarctica," *Metrologia*, vol. 35 (4), pp. 625–629, 1998.
- [29] K. Chance, T. P. Kurosu, and C. E. Sioris, "Undersampling correction for array-detector based satellite spectrometers," *Appl. Opt.*, vol. 44, pp. 1296–1304, 2005.
- [30] B.-C. Gao, P. Yang, W. Han, R.-R. Li, and W. W. Wiscombe, "An algorithm using visible and 1.38 $\mu$ m channels to retrieve cirrus cloud reflectances from aircraft and satellite data," *IEEE Trans. Geosci. Rem. Sens.*, vol. 40, pp. 1659–1669, 2002.
- [31] Newchurch, M. J., Liu, X., Kim, J. H., and P. K. Bhartia, "On the accuracy of Total Ozone Mapping Spectrometer retrievals over tropical cloudy regions," *J. Geophys. Res.*, 106, 32315–32326, 2001.



**Joanna Joiner** received the S.B.(E.E.), S.M.(E.E.), and Ph.D.(E.E.) degrees from the Georgia Institute of Technology in 1987, 1988, and 1991, respectively. Her research focuses on the development of retrieval and data assimilation algorithms for microwave, infrared, and ultraviolet remote sensing instruments. This includes the assimilation of radiances from AIRS and AMSU-A, currently flying on NASA's Aqua satellite, to improve numerical weather prediction. She and her colleagues were the first to demonstrate that information about cloud pressure and chlorophyll content could be retrieved using the properties of Raman scattering in the atmosphere and ocean. This led to the development of algorithms for the Aura OMI. Dr. Joiner currently serves as one of the deputy project scientists for the EOS Aura mission. She is a member of the OMI science team, the American Geophysical Union, and the American Meteorological Society.



**Alexander Vasilkov** received the S.M. degree in Aerospace Engineering and Ph.D. in Physics and Mathematics from the Moscow Institute of Physics and Technology in 1971 and 1975 respectively. His research interests are in the areas of radiative transfer of solar radiation in the atmosphere-ocean system and development of algorithms for retrieving seawater bio-optical parameters from satellite measurements of spectral reflectance. In 1980s he was first to develop a polarization technique for airborne lidar sensing of the vertical profile of seawater turbidity. Currently, he is working on the development of the OMI cloud pressure algorithm that is based on Raman scattering in the atmosphere and ocean.